THE ASTROPHYSICAL JOURNAL, 346:220–231, 1989 November 1

A CO AND FAR-INFRARED STUDY OF THE S254–S258 REGION

MARK H. HEYER
Department of Terrestrial Magnetism, Carnegie Institution of Washington

AND

RONALD L. SNELL, JAMES MORGAN, AND F. PETER SCHLOERB
Five College Radio Astronomy Observatory, University of Massachusetts
Received 1989 February 10; accepted 1989 May 1

ABSTRACT

The molecular cloud associated with compact radio and bright optical H II regions (S254–S258) is studied from observations of ^{12}CO, ^{13}CO, HCN $J = 1$–0 emission obtained at the Five College Radio Astronomy Observatory and far-infrared emission from dust grains measured by *IRAS*. Images of the gas excitation temperature, column density, and kinematics are presented. In addition, the distribution of high-velocity molecular material accelerated by the stellar wind of a newborn star is studied from high signal-to-noise mapping of ^{12}CO emission. The dust component is analyzed by fitting model intensities, derived from a dust mass column density–temperature (σ-T) relation, to the observed far-infrared emission. Such modeling is shown to provide a more complete description of the cold dust component which comprises most of the dust mass than can be determined from the standard single temperature analysis. Local heating of the dust component by newborn massive stars associated with the H II regions of the cloud is inferred from the spatial distribution of temperatures of grains which make the largest contribution to the observed 60 and 100 μm emission. The derived properties of the dust and gas of this cloud are compared with the characteristics of the dust and gas components associated with low-mass star-forming regions.

Subject headings: infrared: sources — interstellar: grains — interstellar: molecules — nebulae: H II regions — nebulae: individual (S254–S258)

I. INTRODUCTION

While comprising only a small fraction of the mass, dust grains play an important role in the global energetics of molecular clouds by regulating the transmission of radiant energy. Gas molecules are heated indirectly by collisions with warm dust grains (Goldreich and Kwan 1974). Thus the relationship between the dust and gas components is critical to the evolution of molecular clouds. However, the properties of the dust component and the coupling between the dust and gas over the extended regions of molecular clouds remain poorly understood and observationally ill-defined. While molecular hydrogen gas is generally well traced by CO emission, direct probes of the dust from observations of thermal grain emission have been generally restricted to known, localized sites of star formation within a molecular cloud. In order to understand the global structure, energetics, and evolution of molecular clouds, it is essential to obtain a more complete description of the dust and gas components over extended size scales.

The *Infrared Astronomical Satellite* (*IRAS*) has surveyed the distribution of far-infrared emission over the entire sky. Thermal emission from dust grains associated with molecular clouds comprise a significant element of the detected radiation. Modeling of the far-infrared emission from molecular clouds provides estimates to the temperatures and column densities of the dust component. Recent studies have revealed a correlation between the column densities of the dust and gas in regions undergoing low-mass star formation (Boulanger and Perault 1988; Snell, Heyer, and Schloerb 1989). In this study, we extend these earlier investigations to regions where massive star formation takes place.

The molecular cloud associated with the optical H II regions S254, S255, S256, S257, and S258, hereafter S254–S258, (Sharpless 1959) is an active site of star formation (Evans, Blair, and Beckwith 1977). The large optical H II regions provide evidence for past star formation while compact radio H II regions and water maser sources are signatures to ongoing massive star formation within the cloud (Israel 1976; Snell and Bally 1986; Lo and Burke 1973). This cloud is part of a larger molecular cloud complex associated with Gem OB1 with a mass of 1.1×10^7 $M_\odot$ (Huang and Thaddeus 1986). Detailed maps of ^{12}CO, ^{13}CO, and HCN $J = 1$–0 emission from this cloud reflect the morphological, thermal, and kinematic properties of the dominant molecular gas component and thus provide an invaluable record of its recent evolution. In addition, we have analyzed the far-infrared emission from this cloud using the co-added survey data from *IRAS* to delineate the characteristics of the dust component.

II. OBSERVATIONS

Evans, Blair, and Beckwith (1977) estimate a distance to the S254–S258 region of 2.5 kpc. We adopt this value in all calculations of physical parameters. All position offsets quoted in this paper are from the 1950 epoch position $(\alpha, \delta) = 06^{h}10^{m}00^{s}, 18°00'00''$.

a) Molecular Spectroscopy

All molecular line observations were obtained with the 14 m telescope of the Five College Radio Astronomy Observatory. A quasi-optical sideband filter and a 256 channel spectrometer with 100 kHz resolution per channel were used with a cryogenic Schottky diode mixer receiver. Calibration of the data was obtained using a chopper wheel which allowed for switching between the sky and an ambient load.

Measurements of the Moon and Jupiter were used to determine the half-power beam width (θ_{FWHP}) and the efficiency on a spatially extended source much larger than the main beam (η_{FSS}). At the rest frequency of ^{12}CO (115 GHz), the values for θ_{FWHP} and η_{FSS} are 45″ and 0.7, respectively. For the HCN $J = 1$–0 transition (88 GHz) θ_{FWHP} and η_{FSS} are 60″ and 0.7, respectively. Temperature ($T_R{}^*$) quoted in this study have been corrected by η_{FSS} which includes ambient temperature losses, effects of Earth's atmosphere, and for forward spillover and scattering losses (Kutner and Ulich 1981). To determine the radiation temperature T_R, for the extended CO emission, no further correction is required since the emission observed here fills the error pattern of the telescope. However, high-velocity CO emission and HCN emission, characterized by much smaller angular sizes ($\approx 5'$), require an additional correction to account for the source coupling efficiency η_c. Therefore, to determine the radiation temperature associated with these components, $T_R = T_R{}^*/\eta_c$, where $\eta_c(5') = 0.7$.

b) *IRAS Co-Adds*

Co-added maps of the 12, 25, 60, and 100 μm emission from the cloud were obtained from the Image Processing and Analysis Center (IPAC). These maps are 2° × 2° in extent sampled at 1′ intervals. The far-infrared images are complicated by background Galactic and zodiacal emission. To remove these components from the maps, a background is determined by fitting a planar surface to the intensities of those regions outside of the known cloud boundaries. The determination of the background level introduces the largest uncertainty in the analysis of the dust. However, the far-infrared emission from the cloud is much larger than the background intensity so the uncertainties associated with the removal of the background are not expected to be significant in our analysis of the cloud.

III. RESULTS

a) *Gas Morphology and Kinematics*

Maps of ^{12}CO and ^{13}CO $J = 1$–0 emission from the molecular cloud associated with S254–S258 were made from 840 observed positions spaced by 1′ on a rectangular grid. The total extent of the ^{12}CO $J = 1$–0 emission is ≈ 20 pc. In Figure 1, we present the distribution of excitation temperature T_{ex}, derived from the observed peak temperature $T_R{}^*$ of the ^{12}CO spectra assuming ^{12}CO emission is optically thick,

$$T_R{}^* = \frac{h\nu}{k}\left[\frac{1}{e^{h\nu/kT_{ex}} - 1} - \frac{1}{e^{h\nu/kT_{BB}} - 1}\right] \mathrm{K}\,, \qquad (1)$$

where T_{BB} is the microwave background radiation temperature. In general, the ^{12}CO $J = 1$–0 transition is thermalized so that T_{ex} is a good measure of the gas kinetic temperature. Most of the gas is characterized by a mean kinetic temperature of 10 K. The location and relative sizes of the optical H II regions are overlayed upon this distribution. The highest gas temperatures of the cloud are spatially coincident with the compact radio H II regions [offset position (0, 0)], where the mean temperature values within the 45″ telescope beam at these positions are 28 K. Warm gas temperatures (20 K) extend southwest along the boundary of the H II regions S254, S256, and S257 and to the east near S258.

The optical depth of the ^{13}CO $J = 1$–0 emission $\tau(^{13}\mathrm{CO})$, is determined from the excitation temperature of ^{12}CO and the ratio of ^{12}CO to ^{13}CO $J = 1$–0 antenna temperatures, assuming equal excitation temperatures for the two transitions. The ^{13}CO column density at each observed position is calculated using the relation

$$N(^{13}\mathrm{CO}) = 2.31 \times 10^{14}\,\frac{T_{ex}\,\Delta v\,\tau(^{13}\mathrm{CO})}{1 - e^{-h\nu/kT_{ex}}}\ \mathrm{cm}^{-2}\,, \qquad (2)$$

where Δv is the full line width of the ^{13}CO line measured at half-maximum. In Figure 2, the distribution of ^{13}CO column density is displayed. The column density distribution peaks at the position of the compact radio H II regions and where emission from probes of dense gas such as NH_3 and HCN are detected (Ho, Martin, and Barrett 1981; Richardson *et al.* 1984). This region of enhanced gas column density is located between the optical H II regions S255 and S257. The morphology of this central core is elongated along a north-south direction and is similar to the distribution of submillimeter continuum emission (Jaffe *et al.* 1984; Mezger *et al.* 1988); however, secondary emission peaks found in these studies are

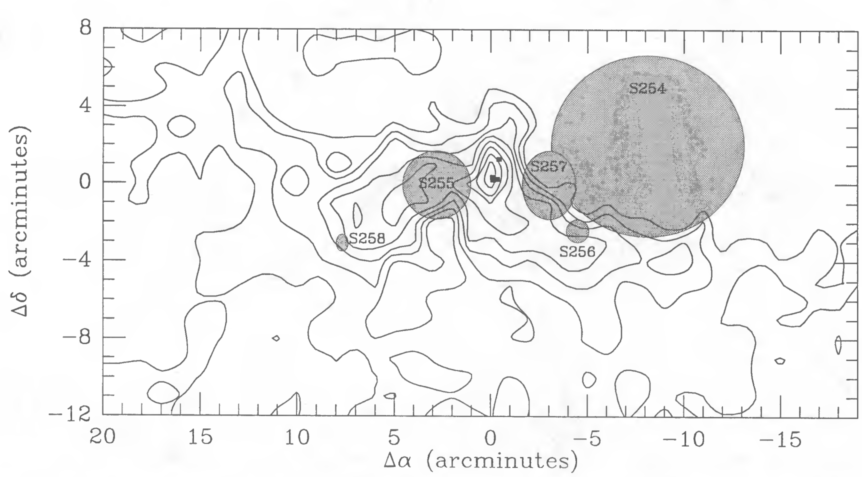

FIG. 1.—Map of the gas excitation temperature derived from the peak ^{12}CO $J = 1$–0 antenna temperature. The contour levels are 9, 12, 15, 18, 21, 24, 27, and 30 K. Cooler gas ($T < 9$ K) is located toward the southeastern boundary of the map. The half-tone circles overlayed upon the map denote the positions and approximate sizes of the optical H II regions. The filled squares mark the positions of the compact radio H II regions identified by Snell and Bally (1986). The warmest gas ($T_{ex} > 20$ K) is associated with the compact H II regions near the offset position (0, 0).

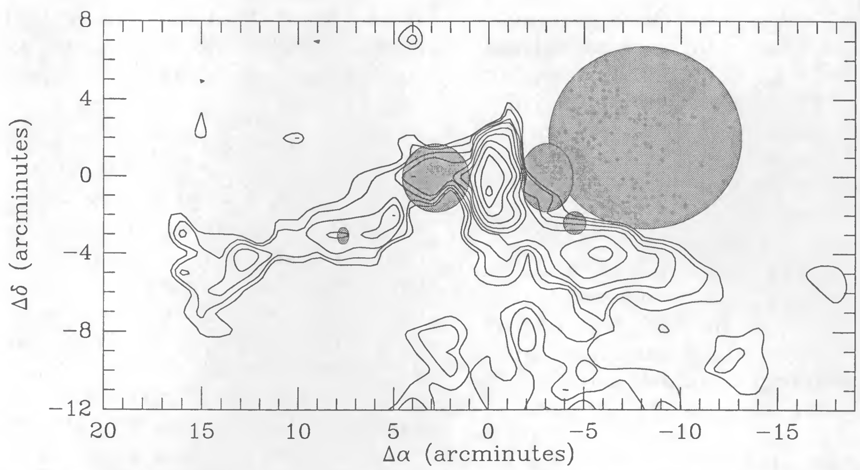

FIG. 2.—Map of ^{13}CO column density derived from the ratio of ^{12}CO to ^{13}CO intensities and assuming equal excitation temperatures for the two transitions. ^{13}CO is detected over a larger region than is shown by these contour levels which emphasize the regions with the highest gas column densities. The contour levels are spaced logarithmically between 6.5×10^{15} and 6.5×10^{16} cm^{-2}. The molecular gas is highly condensed within the central core region.

not resolved by our observations. The cloud branches to the southeast and southwest along narrow extensions. Each extension has several local column density maxima. Diffuse ^{13}CO emission extends to the south beyond the boundaries of the map. While there is no detected ^{13}CO emission in the direction of S254, the outer radio continuum isophotes of S254, S256, and S257 (Israel 1976) coincide with the sharp ridge of enhanced column density along the western arm of the cloud. A total mass of 2.7×10^4 $M_\odot$ of molecular material is determined from the summation of ^{13}CO column densities over the observed region and assuming an abundance of ^{13}CO to H_2 of 1×10^{-6}. A large fraction of the cloud's mass (14%) is condensed within a region $5' \times 7'$ in extent and centered on the compact H II region position.

Investigation of gas kinematics provides a more complete description to the internal structure of the cloud. The radial component of the internal motions of molecular material are presented in Figure 3 as a sequence of maps of the ^{13}CO $J = 1$–0 antenna temperatures within velocity intervals spaced by 0.5 km s^{-1}. The cloud exhibits peculiar large-scale kine-

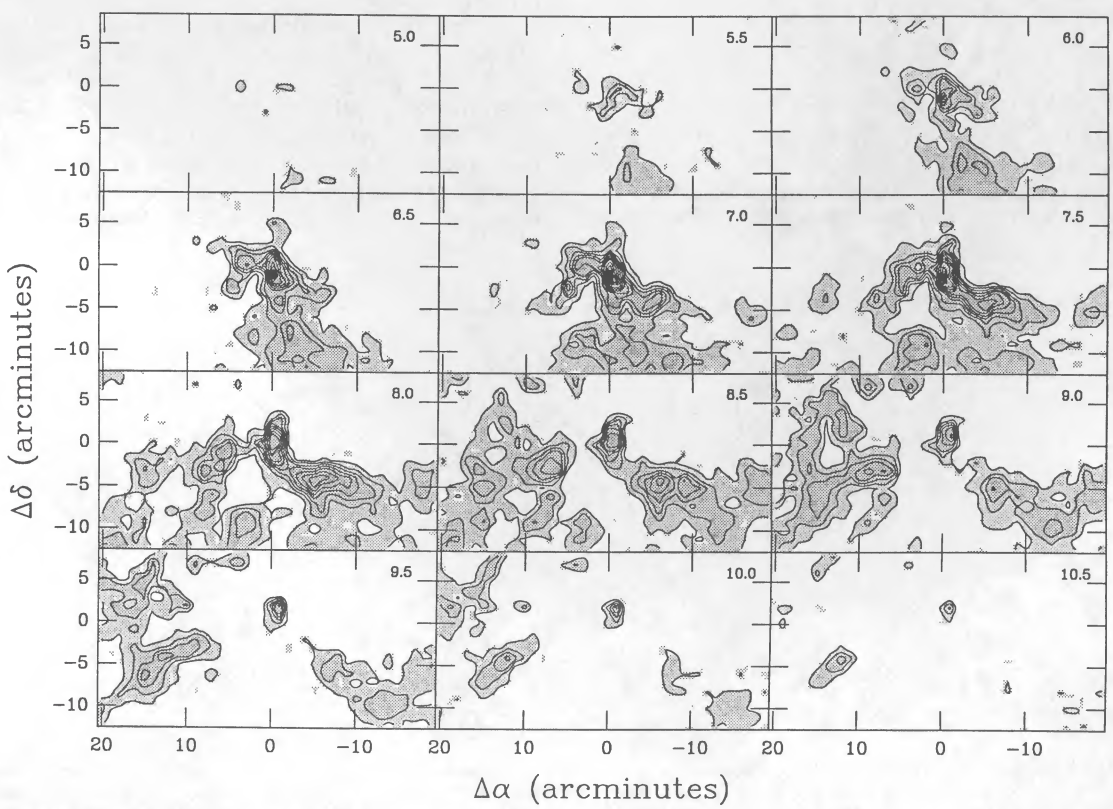

FIG. 3.—A sequence of maps showing the antenna temperature (T_R*) of ^{13}CO $J = 1$–0 emission within velocity intervals 5 to 10.5 km s^{-1}. The contour levels for each map are 1, 2, 3, 4, 5, 6, 7, 8, 9, 10 K. The cloud is composed of several internal clumps moving with large relative velocities with respect to one another.

matics. At low velocities (5.5–6.5 km s^{-1}), most of the emission is associated with the central core region with extended but diffuse emission to the south. At intermediate velocities (7–8 km s^{-1}), extended emission is detected to the southeast and southwest of the central core. These extended features shift to greater distances from the central core as velocities increase from 8 to 10 km s^{-1}.

Two important kinematic features associated with the central core are manifest in Figure 3 relative to the remainder of the cloud. First, the broadest lines are found toward the central core where ^{13}CO emission is detected over the velocity range 5.5–10.5 km s^{-1}. ^{12}CO emission is detected from this region over an even larger velocity interval. Second, there is a systematic shift with increasing velocity in the position of the emission centroid from south to north. Such velocity shear has been previously detected from high-density tracers such as NH_3 and HCN (Ho, Martin, and Barrett 1981; Richardson *et al.* 1985). However, inspection of the line profiles of ^{13}CO $J = 1–0$ emission spectra from the northern region of the central core reveals two distinct velocity components. These same two velocity components, at 6.0 km s^{-1} and 8.0 km s^{-1}, are also present in the HCN $J = 4–3$ line profiles observed toward these lines of sight (Richardson *et al.* 1985). These two-velocity components likely delineate several condensations within the core.

In order to probe the dense gas within the central core more directly, we have mapped the distribution of HCN $J = 1–0$ emission from this region at 1′ spacing. This transition requires densities greater than 10^5 cm^{-3} for excitation, and therefore, is a direct probe of high-density regions. In Figure 4, we present the integrated intensity of the HCN emission. The maximum HCN emission is found toward the compact H II regions with secondary peaks toward S258 and to the southwest of the central core region. This distribution is similar to that of the ^{13}CO column density and suggests that these locations are regions of both enhanced space and column density.

High-velocity material accelerated by stellar winds from newborn stars contributes an additional component to the kinematic structure of molecular clouds. Bally and Lada (1982) identify the central core region as a site of high-velocity ($\Delta v = 26$ km s^{-1}) ^{12}CO $J = 1–0$ emission. In order to determine the extent of this energetic activity, we have mapped the distribution of the high-velocity CO emission at 0ʹ.5 spacing. While the line shapes are generally symmetric, weak high-velocity emission is present over an angular size scale of 4′ (2.9 pc). The extent of this outflow is large compared to most known regions of accelerated molecular material (Lada 1985). Maps of the blueshifted and redshifted emission integrated over the intervals 0–5 and 10–15 km s^{-1} respectively are shown in Figure 5. The angular offset between the redshifted and blueshifted emission may in part be due to the two velocity components at 6 and 8 km s^{-1} in the core. The solid squares identify the positions of the 6 cm radio continuum sources detected by Snell and Bally (1986). The physical parameters of the outflow have been calculated assuming optically thin high-velocity emission and a CO to H_2 abundance of 10^{-4}. The stellar mass-loss rate is calculated assuming conservation of momentum and a stellar wind velocity of 100 km s^{-1}. The values for these outflow properties are listed in Table 1. The stellar origin of the outflow is likely one of the sources responsible for the radio continuum emission detected by Snell and Bally (1986).

b) Far-Infrared Emission

Extended (30′ × 15′) emission in all four *IRAS* bands is associated with the S254–S258 cloud region. In Figure 6, the distributions of intensities from all four bands are shown. The far-infrared emission is centrally peaked on the position of the compact H II regions and peak ^{13}CO column density. A significant fraction of this peak intensity is associated with a source (06100+1800) identified in the *IRAS* Point Source Catalog (1985). From high-resolution radio continuum observations Beichmann, Becklin, and Wynn-Williams (1979) and Snell and Bally (1986) identify several newborn stars within the *IRAS* beam at this location. A secondary point source (06106+1756) is associated with S528 which accounts for the local intensity peak seen most prominently at 25 μm to the southeast of the central core region. There is far-infrared emission in all four bands from the S254 region from which there is no detectable CO emission.

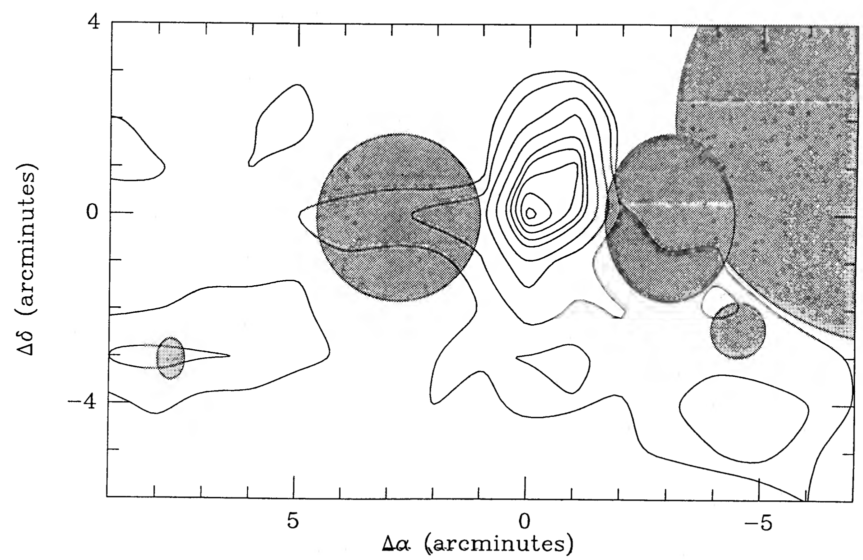

FIG. 4.—A map of the integrated HCN $J = 1–0$ emission tracing the high-density gas associated with the central core region. The contour levels are 2, 4, 8, 12, 16, 18, 20, 22, 24 K km s^{-1}. Regions of enhanced column density as delineated by ^{13}CO $J = 1–0$ emission are regions of high volume density as well.

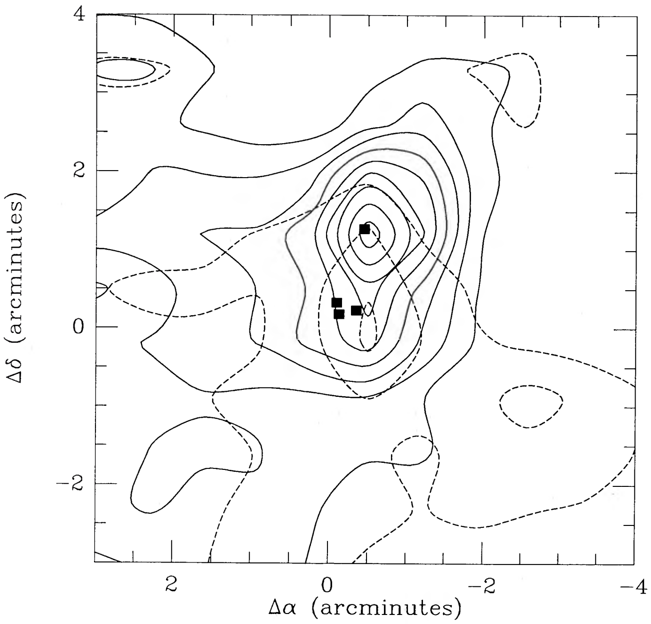

FIG. 5.—A map of the high-velocity ^{12}CO $J = 1\text{–}0$ emission excited by a stellar wind from a newborn star within the central core. The contour values for the red (*solid*) and blueshifted (*dotted*) intensity distributions are 4, 7, 10, 13, 16, 19, 22, 25, 28 K km s^{-1}. The square points denote the positions of 6 cm radio continuum sources detected by Snell and Bally (1986).

The total measured luminosity from all four *IRAS* bands is 9.8×10^4 $L_\odot$ with most of the energy (44%) detected within the 60 μm band. An estimate of the total far-infrared luminosity associated with the dominant cold component is calculated using the 60 and 100 μm flux densities and correcting for out-of-band emission between 1 and 500 μm (Lonsdale *et al.* 1985). Based upon the mean color temperature of 35 K, inferred from the ratio of 60 μm emission to 100 μm emission, the extrapolated luminosity emitted by this cold dust component of the S254–S258 cloud is 1.0×10^5 $L_\odot$.

TABLE 1

PHYSICAL PROPERTIES OF THE MASS OUTFLOW

Outflow Property	Calculated Value
Mass ($M_\odot$)	25.8
Momentum ($M_\odot$ km s^{-1})	87.9
Energy (ergs)	1.7×10^{45}
Velocity (km s^{-1})	3.4
Size (pc)	1.8
τ (10^5 yr)	5
Force ($M_\odot$ km s^{-1} yr^{-1})	1.8×10^{-4}
Luminosity ($L_\odot$)	0.06
$\dot{M}_*$ ($M_\odot$ yr^{-1})	1.8×10^{-6}

c) *Gas-to-Dust Comparison*

The data presented in § III*a*, *b* are tracers of the gas and dust components associated with the S254–S258 molecular cloud. A comparison between these measures of cloud structure may provide insight into the coupling between these cloud components. In Figure 7, we present a point to point comparison of the 100 μm intensity $I_{100\,\mu m}$, to ^{13}CO integrated intensity, $\int T(^{13}CO)dv$. With the exception of the central core region where both $I_{100\,\mu m}$ and ^{13}CO emission are large, there is only a moderate correlation of the far-infrared emission with the large-scale distribution of CO emission. There are regions with substantial ^{13}CO emission but with $I_{100\,\mu m} < 2 \times 10^{-6}$ W m^{-2} sr^{-1}. Toward S254 where the gas is presumably ionized and possibly dispersed by the expansion of the H II region, there is no detected CO emission but moderately bright far-

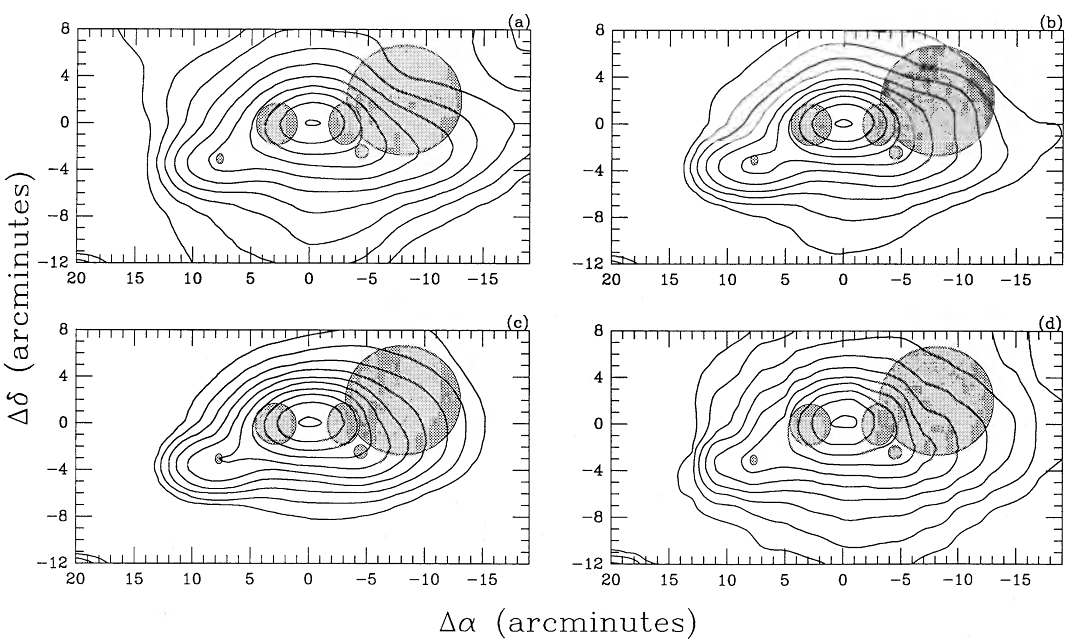

FIG. 6.—Distribution of the far-infrared emission from the S254–S258 cloud as measured by *IRAS* at (*a*) 12 μm, (*b*) 25 μm, (*c*) 60 μm, and (*d*) 100 μm. The contour levels for each band are spaced logarithmically and range between the values 1.5×10^{-7} to 1.5×10^{-5} W m^{-2} sr^{-1} at 12 μm, 1.75×10^{-7} to 1.75×10^{-5} W m^{-2} sr^{-1} at 25 μm, 6.5×10^{-7} to 6.5×10^{-5} W m^{-2} sr^{-1} at 60 μm, 3.5×10^{-7} to 3.5×10^{-5} W m^{-2} sr^{-1} at 100 μm. Much of the emission in each band arises from an unresolved source within the central core.

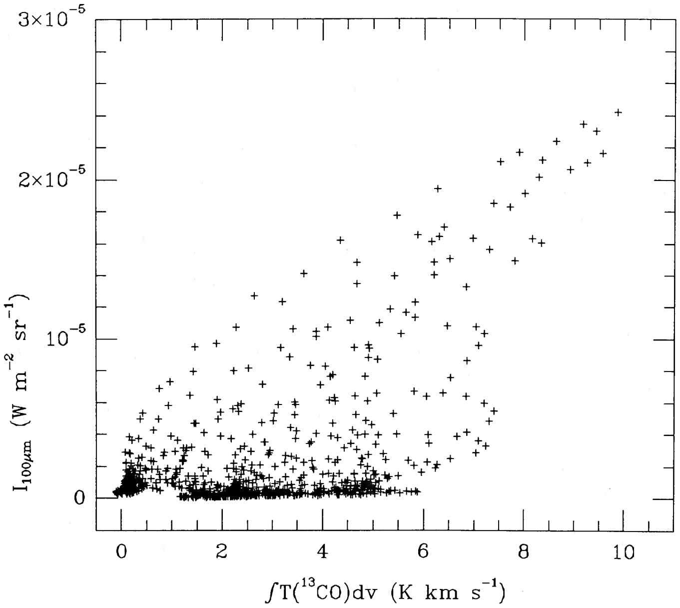

FIG. 7.—A point-to-point comparison between the 100 μm intensity and integrated ^{13}CO $J = 1$–0 emission. An average ratio between these quantities over the entire cloud is 8.3×10^{-7} W m^{-2} sr^{-1} (K km s^{-1})$^{-1}$.

infrared emission from dust within the H II region. A mean ratio between the 100 μm intensity and ^{13}CO $J = 1$–0 integrated intensity is estimated from the summation of these values over the region mapped. The calculated ratio is 8.3×10^{-7} W m^{-2} sr^{-1} (K km s^{-1})$^{-1}$ averaged over the entire cloud and 1.9×10^{-6} W m^{-2} sr^{-1} (K km s^{-1})$^{-1}$ in the central $5' \times 7'$ region. Snell, Heyer, and Schloerb (1989) determine a ratio of 2×10^{-8} W m^{-2} sr^{-1} (K km s^{-1})$^{-1}$ in the Taurus clouds.

IV. DUST MODEL

In order to make a proper comparison between the dust and gas components, it is necessary to extract physical quantities (temperature and column density) from the measured far-infrared emission. Relative intensities between bands provide an approximate measure of the temperature of the dust component responsible for the observed emission. Color temperatures $T(\lambda_1/\lambda_2)$ have been calculated from the ratios of 12 μm to 25 μm emission, 25 μm to 60 μm emission, and 60 μm to 100 μm emission, assuming an emissivity law of λ^{-1} appropriate for $\lambda < 250$ μm (Hildebrand 1983). Mean values for the derived $T(12/25)$, $T(25/60)$, and $T(60/100)$ distributions are 180, 67, and 35 K, respectively. Such a large range in dust temperatures is expected given the distribution of grain sizes required to account for the interstellar extinction curve (Mathis, Rumpl, and Nordsieck 1977) and the dependence of grain optical properties upon grain size. For a given radiation field, the equilibrium temperature of small grains is warmer than that of larger grains, therefore, 12 and 25 μm emission may more accurately trace the small-size grain population. Moreover, the temperature of small grains increases to large values (500–1000 K) immediately following the absorption of a UV or visual photon due to the low specific heats of these grains relative to the energy of the absorbed radiation (Purcell 1976). Draine and Anderson (1985) and Boulanger *et al.* (1988) have shown that such temperature fluctuations of small grains not in thermal equilibrium with the ambient radiation field can make significant contributions to the 12, 25, and possibly 60 μm emission. The presence of long-chain molecules, inferred from near-infrared absorption features, can also contribute significant emission within the *IRAS* bands (Puget, Leger, and Boulanger 1985). Since small grains do not constitute much of the mass associated with the dust component, the derived color temperature, especially at lower wavelengths, may not accurately characterize the thermal properties of most of the dust mass. Finally, Snell, Heyer, and Schloerb (1989) discuss the uncertainties in deriving color temperatures and dust opacities from observed intensities in regions where temperature gradients are likely to be present due to heating sources. In general, the derived color temperature is weighted toward the highest temperature along the line of sight and therefore overestimates the temperature of dust which may comprise most of the dust mass. Thus, since an *overestimate* to the color temperature to derive the dust opacity results in a gross *underestimate* of the true dust opacity present within the cloud, it is clear that a new approach to the estimation of dust temperatures and opacities is required.

Given the known large gradients in the dust temperature and therefore, the inadequate description of the dust components by a single temperature, we have modeled the far-infrared emission from an assumed mass column density–temperature (σ-T) relation. This relation is varied in order to fit the observed far-infrared emission at each point in the cloud. The model intensity is calculated from

$$I(\lambda) = \frac{Q}{a\rho} \int_{15\,\mathrm{K}}^{250\,\mathrm{K}} \left(\frac{d\sigma}{dT}\right) dT \int_{\mathrm{bandpass}} d\nu B_\nu(\nu, T) R_\lambda(\nu) . \quad (3)$$

$R_\lambda(\nu)$ is the response function of the *IRAS* detector of the band λ. These values for Q/a at each band are from Draine (1985) and a grain density of 3 g cm^{-3} is assumed. After investigating several candidate functional forms for $d\sigma/dT$, we have found that the function

$$\frac{d\sigma}{dT} = \sigma_0 \exp\left(-\frac{(T-15)}{T_0}\right) + \Sigma_0 \text{ g cm}^{-2}\text{ K}^{-1} . \quad (4)$$

can adequately fit the observations. At the high-temperature limit, this form approaches a constant value Σ_0 and therefore represents a crude approximation to the amount of nonequilibrium dust grains. We attach no physical significance to the functional form of the σ-T relation used in this study. Our interest is focused only upon the amount of dust that is necessary at each temperature to fit the observed far-infrared intensities. The primary limitations to the model are the chosen temperature limits of integration. A comparable fit to the data can be obtained using a lower (higher) value for the lower limit which would result in a larger (smaller) value for σ_0. In fits to our data, we find that the 12 μm emission is systematically *underestimated* by $\approx 5\%$, and the 25 μm emission is generally *overestimated* by $\approx 10\%$. Such large residuals are clearly due to the inadequate description to the amount of nonequilibrium grains as a constant function of temperature. The 60 and 100 μm intensities are fitted to less than 1%. However, such an accurate fit is expected given that these two bands are modeled by the two-parameter exponential term in equation [4].

From modeling of the far-infrared emission, we can estimate the temperatures of dust grains which make the largest contribution to the intensity within each *IRAS* band. In Figure 8, we present the intensity contribution $I_\lambda(T_i)$ averaged over the cloud from the dust component at temperature T_i. The 12 μm

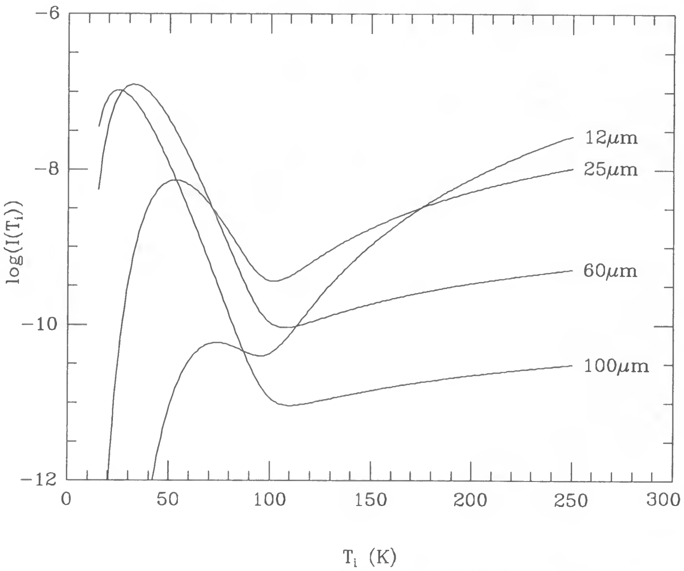

FIG. 8.—The contribution curve averaged over the cloud showing the model intensity produced by the dust component as a function of temperature. The 12 μm emission is dominated by the hottest dust temperatures used in the model. The 25 μm emission is generated from an equal contribution by the cold and hot dust components. Both the 60 and 100 μm emission are dominated by the cold dust component which comprises most of the dust mass.

emission is dominated by dust with temperatures greater than 200 K which is clearly an artifact of our model in which the mass column density of nonequilibrium grains is constant with temperature while the Planck function is an increasing function of temperature. At 25 μm, the contributions from hot, nonequilibrium grains and the cold dust component are approximately equal and the 60 and 100 μm emissions are dominated by the cold dust component. We define an intensity-weighted temperature to describe the temperature of the dust most responsible for the observed far-infrared emission as

$$T_\lambda = \frac{\int I(\lambda, T) T\, dT}{\int I(\lambda, T) dT}\ \mathrm{K}\ . \tag{5}$$

Since the model 12 μm intensity is simply an increasing function of temperature, the associated intensity weighted temperature is not well defined at this band. The mean values of T_{25}, T_{60}, and T_{100} are 194, 34, and 25 K, respectively. It is clear that the simple color analysis described earlier cannot adequately describe the far-infrared emission since each band is sensitive to a different temperature component. The intensity-weighted temperature distributions for the 25, 60, and 100 μm bands are presented in Figure 9. The temperature of dust contributing most of the observed 60 and 100 μm emission increases toward the cloud center and S258. However, the dust grains responsible for the 25 μm emission from the central core appear cooler than the dust contributing to the 25 μm emission near the edge of the cloud. Such an inverted temperature gradient relative to the distributions of T_{60} and T_{100} can be understood by the larger contribution from the cold dust component to the 25 μm emission from the central core where the column densities are large. The larger contribution of this cold component reduces the derived mean temperature relative to the edge of the cloud where the intensity is more dominated by hot, nonequilibrium dust grains.

V. DISCUSSION

a) Gas Mass-to-Dust Mass Ratio

From previous studies of nearby, cold dark clouds with 60 to 100 μm color temperature $\approx$23 K, a linear relationship is found between the dust and gas mass column densities (Snell, Heyer, and Schloerb 1989; Boulanger and Perault 1988). However, the derived relationships in Snell, Heyer, and Schloerb (1989) suggests only a small fraction (2%–5%) of the dust contributes to the far-infrared emission detected by *IRAS*. A similar analysis of the 60 and 100 μm emission from the S254–S258 cloud leads to a higher average dust temperature (35 K), but to the same conclusion that only a small fraction of the dust contributes to the *IRAS* emission. In the earlier studies it was assumed that the remaining dust in these regions is at sufficiently low temperatures and therefore does not contribute much emission within these wavelength bands. The fraction of the dust contributing to the emission from the S254–S258 cloud can be better estimated using our model which accounts for a continuum of dust temperatures along the line of sight.

In Figure 10, we present the mass column density of dust

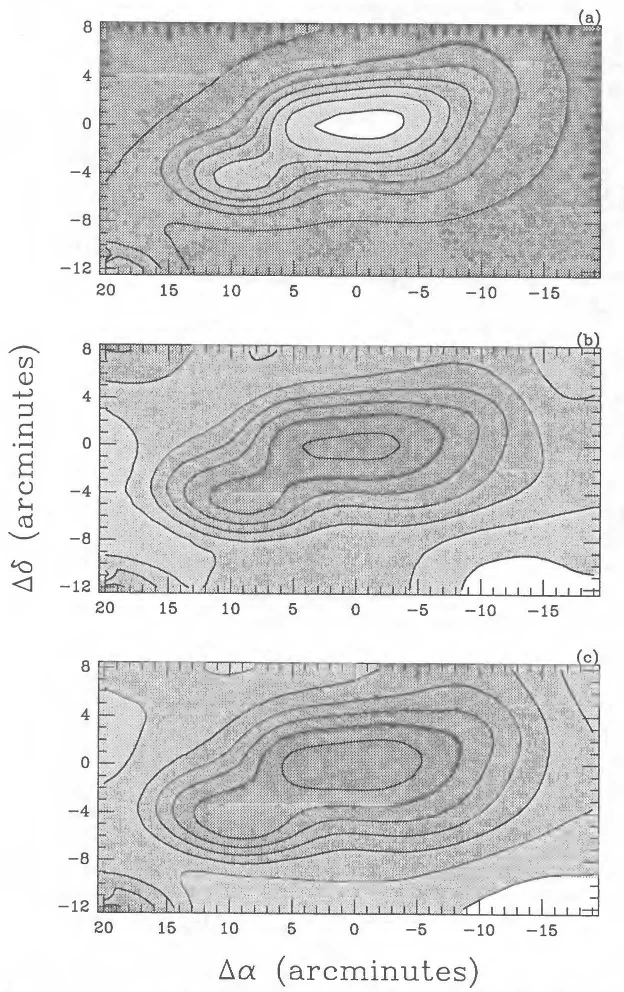

FIG. 9.—The spatial distribution of the intensity weighted temperatures at (*a*) 25 μm (contour levels: 145, 155, 165, 175, 185, 195, and 205 K), (*b*) 60 μm (contour levels: 29, 31, 33, 35, 37, 39, and 41 K), and (*c*) 100 μm (contour levels: 20, 22, 24, 26, 28, 30, and 32 K). Half-tone scaling illustrates an increase in temperature from light to dark.

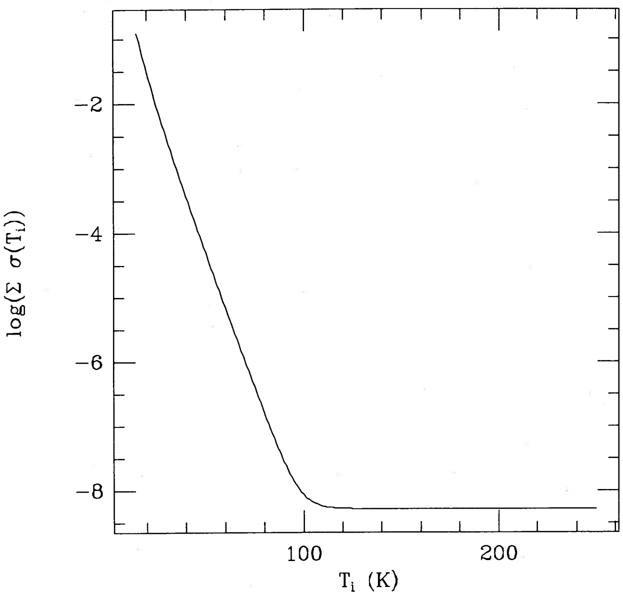

FIG. 10.—The mass column density of dust summed over the cloud as a function of temperature derived from modeling of the far-infrared emission.

derived from modeling the far-infrared emission and summed over the entire cloud as a function of temperature. The fraction of dust hotter than 50 K is extremely small but at lower temperatures it is intrinsic to our model that the amount of dust increases with decreasing temperature to the 15 K lower limit. Because the dust emission at the *IRAS* wavelengths declines exponentially for temperatures below 15 K (see Fig. 8), one can add arbitrary amounts of dust colder than 15 K without affecting the fits to the data. To derive the total dust mass requires one to be certain that at low temperatures, the dust component contributes to the observed emission. Figure 8 demonstrates that dust even at 15 K is making a significant contribution to the observed emission. Thus, the total mass column density σ_{dust} is obtained by integrating over the entire temperature interval used in deriving the model intensities,

$$\sigma_{\text{dust}} = \int_{15\,\text{K}}^{250\,\text{K}} \left(\frac{d\sigma}{dT}\right) dT \text{ g cm}^{-2} . \tag{6}$$

The spatial distribution of the estimated total mass column density of dust from this model is presented in Figure 11. It is highly condensed toward the central core region. The spatial distributions of the dust component integrated over cold, warm, and hot temperature intervals are similar indicating that dust grains at all temperatures are present throughout the cloud.

To determine the fraction of dust mass contributing to the observed far-infrared emission in this study, we compare the dust mass column density σ_{dust} derived from our modeling, to the gas mass column density σ_{H_2}, derived from CO observations convolved to the *IRAS* 100 μm resolution and assuming a ^{13}CO to H_2 abundance of 1×10^{-6}. A point-to-point comparison between these quantities is shown in Figure 12. An equal weighting least-squares fit to the data points with $\sigma_{H_2} >$ 0.01 g cm^{-2} provides the following relation:

$$\sigma_{H_2} = (154 \pm 6)\sigma_{\text{dust}} + (0.016 \pm 0.0004) \text{ g cm}^{-2} . \tag{7}$$

Alternatively, we could estimate the gas-to-dust ratio using the total mass of the gas and dust in the cloud. From the ratio of these mass components, we derive a mean gas-to-dust mass ratio of 540 for the entire cloud and 229 for the central $5' \times 7'$ core region. If the true gas-to-dust mass ratio is ≈ 100 (Bohlin, Savage, and Drake 1978), then 19% and 44% of the dust is modeled in the core and the entire cloud respectively. Thus, by modeling the far-infrared emission with a distribution of grain temperatures, a larger fraction of the dust is probed than is inferred from the standard single-temperature analysis. It is likely that the emission from the cold dust component in dark clouds is also detected by *IRAS* (Snell, Heyer, and Schloerb 1989), but the analysis used in this previous study failed to account for the temperature distribution present in interstellar clouds and therefore underestimated the amount of dust present.

b) *Dust and Gas Heating*

Most of the radiant energy injected into the cloud either internally by newborn stars or externally by the interstellar radiation field is emitted at wavelengths less than 1 μm and is processed through the dust component. Therefore, the observed dust temperature spatial distributions are direct signatures to the flow of energy within the cloud and thus should

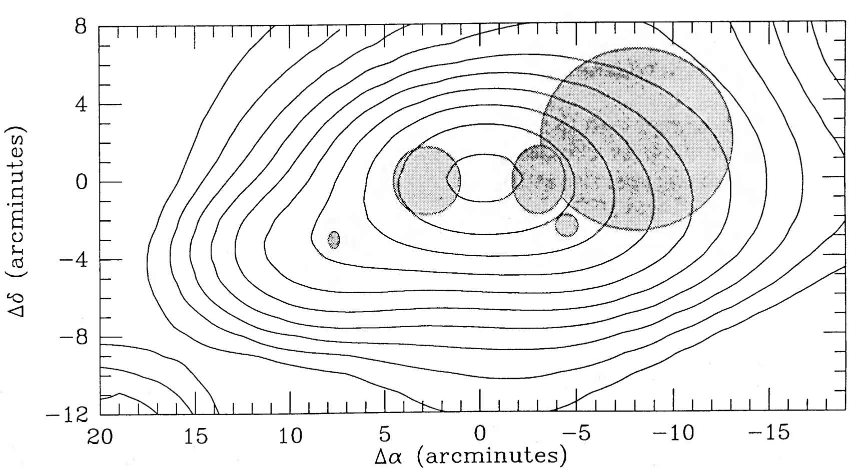

FIG. 11.—The spatial distribution of the total mass column density of dust σ_{dust}, integrated over the temperature interval 15 to 250 K. The contour levels are spaced logarithmically between the range 1×10^{-6} and 2.5×10^{-4} g cm^{-2}.

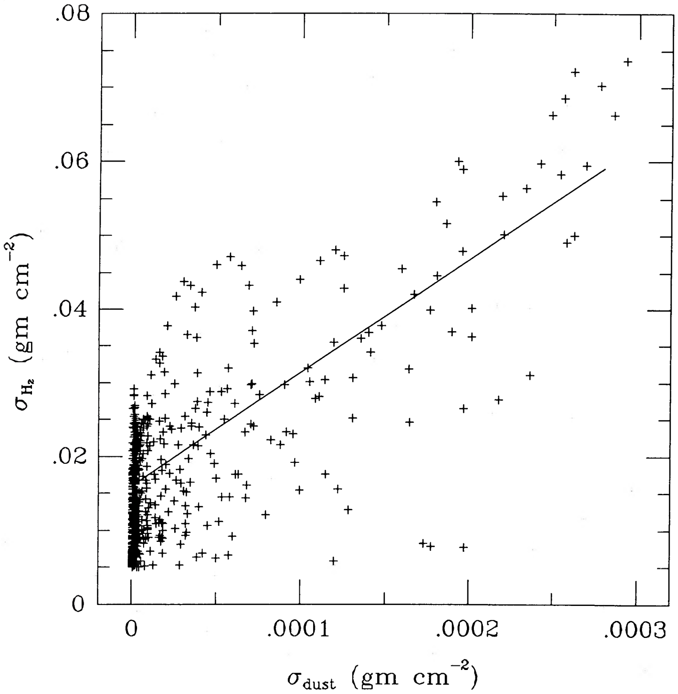

FIG. 12.—A point-to-point comparison between the gas mass column density σ_{H_2}, and dust mass column density σ_{dust}. The linear fit to these data implies an average gas-to-dust ratio of 154 ± 6.

identify the dominant heating sources. The temperature distributions T_{60} and T_{100} (see Fig. 9) identify two regions within the cloud as sources of dust heating; the central core region (which contains embedded compact H II regions and the optical H II regions S255 and S257) and S258 to the southeast of the core. Estimates of the total luminosities of the sources responsible for the four compact H II regions based on the number of UV ionizing photons have been tabulated by Snell and Bally (1986) to be $2.7 \times 10^4 L_\odot$. Equivalently, Evans, Blair, and Beckwith (1977) estimate a luminosity of $5 \times 10^4 L_\odot$ for each star responsible for S255 and S257. The *IRAS* resolution element is insufficient to distinguish which source within the central core contributes most of this energy. The total luminosity emitted from the cloud based on the observed fluxes is $10^5 L_\odot$ which suggests that the stars responsible for the compact H II regions are insufficient to heat the entire cloud. The global heating of the cloud may be dominated by the central stars in S255, S256, and S257, a conclusion reached by Evans *et al.*

To determine if radiation fields associated with these stellar sources are sufficient to heat the dust, we have compared the radial profiles of the intensity-weighted temperature at 100 μm to models of dust heating. Scoville and Kwan (1976) have calculated the dust temperature as a function of distance from a luminous source including the effects of dust reradiation as a secondary heating source. In addition, they derive an analytical expression for the upper limit of the dust temperature as a function of distance from a star by assuming no absorption of the stellar radiation field. The profile of T_{100} with distance from the central core region is shown in Figure 13. Points east of $\alpha(1950) = 06^h10^m34^s$ have been excluded to avoid confusion with regions heated by the central star exciting S258. The broad plateau of T_{100} values between 0′ and 4′ is due to the low resolution of the *IRAS* beam and the distribution of luminous sources around the central core. The upper limit to the grain temperature at each distance derived by Scoville and Kwan (1976) is also displayed using the emissivity values tabulated by Draine (1985) for grain radii 0.01 to 0.1 μm which may characterize the sizes of grains responsible for most of the observed 100 μm emission and assuming a total internal luminosity of $1.27 \times 10^5 L_\odot$ present within the central core. The values of T_{100} are bounded by the model upper limit temperatures of grains with these emissivities. Moreover, the grain temperatures appear to radially decrease at a rate comparable to that derived by Scoville and Kwan (1976) for an emissivity law $Q(\lambda) \propto \lambda^{-1}$.

The degree to which the dust and gas components are coupled may be inferred from the spatial correlation between the gas excitation temperature and the dust temperature. However, we emphasize that a *spectrum* of dust temperatures are necessary to fit the observed far-infrared intensities. The parameter T_{100} characterizes dust temperatures only within a narrow range of this spectrum. In addition, T_{100} is an intensity-weighted temperature where T_{ex} is likely a mass-weighted temperature (see Appendix). Nevertheless, the highest gas temperatures (≈ 30 K) are found in the central core region where the distribution of T_{100} also peaks (30 K) and where the highest densities of both the dust and gas components are located. In this region, the gas component appears to be well coupled to the radiation field by frictional heating with warm dust grains (Goldreich and Kwan 1974). In the outer regions of the cloud, gas temperatures decrease more rapidly than the dust temperatures at larger distances and there is no observed spatial correlation. In these outer regions of the cloud where the densities are low, the gas and dust are not well coupled.

c) Star Formation and Cloud Evolution

The presence of both large optical and compact H II regions, bright infrared sources, and OH and H_2O masers attest to the

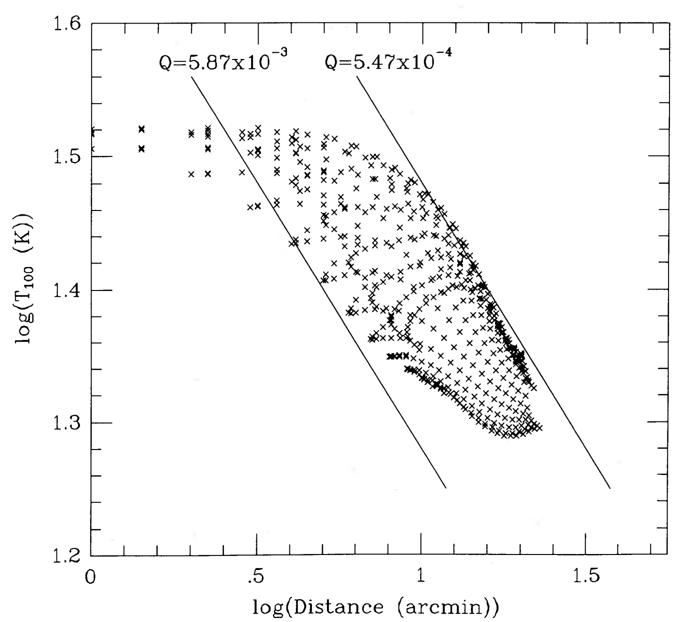

FIG. 13.—The radial profile of the intensity-weighted temperature at 100 μm. The solid lines are the analytical radial profiles to the upper limit of dust temperatures derived by Scoville and Kwan (1976) assuming no opacity between the star and dust grain and grain emissivities of 5.87×10^{-3} and 5.47×10^{-4}.

formation of massive stars within the S254–S258 molecular cloud. Low-mass stars may also be forming but the light from these stars is overwhelmed by the radiation from high-mass stars; therefore, it is not possible to identify these sites from these observations. Since most of the present massive star-formation activity is concentrated within the central $5' \times 7'$ (3.6 pc $\times$ 5.1 pc), it is useful to compare the properties of this region with the global properties of the cloud. In Table 2, we have tabulated the physical properties and mean temperature values over the entire cloud and over the central $5' \times 7'$ core region. The central core, although accounting for only 4% of the projected area, contains 14% of the mass of the gas component and radiates 34% of the total infrared luminosity. Thus one of the striking differences between the core and the cloud is the luminosity-to-mass ratio. If newborn stars are primarily responsible for the heating of the dust component, as is clearly the case in this cloud, then the luminosity-to-mass ratio may provide a measure of the star-formation efficiency. For the central core, the value of L/M is 8.7 $L_\odot/M_\odot$, while the average value for the cloud is 3.7 $L_\odot/M_\odot$. The cloud average is similar to the level of star-formation activity averaged over the Galactic disk (Scoville and Good 1987) where the value of L/M is 2.8 $L_\odot/M_\odot$. The core, on the other hand, is more typical of regions of enhanced high-mass star formation, such as W51 or M17 (Scoville and Good 1987; Mooney and Solomon 1988).

It is interesting to compare the properties and morphology of star formation in this giant molecular cloud with the characteristics of a region of similar size and mass that is producing only low-mass stars. The best studied low-mass star-forming region is the Taurus cloud complex which has nearly identical size (30 pc) and mass (3×10^4 $M_\odot$; Ungerechts and Thaddeus 1987) to the S254–S258 molecular cloud. The average value of L/M is 0.3 $L_\odot/M_\odot$ in the Taurus clouds (Snell, Heyer, and Schloerb 1989), but unlike the S254–S258 cloud, the luminosity is largely due to far-infrared emission from dust grains heated by the interstellar radiation field. The most notable distinction between the two clouds is their morphology. In the S254–S258 cloud, the distribution of gas is concentrated in the central core region, in contrast to Taurus where gas clumps are distributed uniformly over the cloud complex.

Cloud models presented by Lizano and Shu (1988) suggest that high-mass star formation and low-mass star formation result from different evolutionary paths of the parent molecular cloud. Low-mass star-forming regions such as the Taurus complex have remained close to viral equilibrium, supported primarily by the interstellar magnetic field (Moneti *et al.* 1984; Heyer *et al.* 1987). In giant molecular clouds, rapid large-scale collapse of the cloud may result from the enhanced gas column densities and therefore, larger self-gravitational forces. However, the mechanism responsible for the larger initial column densities of the cloud is uncertain.

TABLE 2

Physical Parameters of the Central Core and Cloud

Parameter	Core	Cloud
T_{ex} (K)	16	9
T_{25} (K)	152	194
T_{60} (K)	40	34
T_{100} (K)	32	25
M_{H_2} ($M_\odot$)	3900	2.7×10^4
M_{dust} ($M_\odot$)	17	50
L_{FIR} ($L_\odot$)	3.4×10^4	1.0×10^5

It was suggested by Loren (1976) and more recently by Scoville, Sanders, and Clemens (1986) that massive star formation may be triggered by cloud-cloud collisions. The highly condensed nature of massive star-forming regions such as the central core of the S254–S258 cloud may be a direct consequence of these collisions. Since the S254–S258 cloud is but one of many molecular clouds which constitute the Gem OB1 giant molecular cloud complex, such collisions may be frequent events over the lifetime of the cloud. The gas kinematics provide a fossil record of the cloud's evolution within the last crossing time scale. The spatial maps of the S254–S258 cloud at various velocities (see Fig. 3) reveal several clumps at different velocities. The interaction between two or more of the clumps could plausibly, although not uniquely, explain the kinematics seen in this cloud.

Another plausible explanation for the origin of the massive core in the S254–S258 cloud is the compression of cloud material by neighboring H II regions. Elmegreen and Lada (1977) proposed that massive star formation propagates through clouds as a result of gas compression by shocks from adjacent H II regions. The location of the central core between S255 and S257 (see Figs. 1 and 2) suggest that this region could have been a product of the expansion of these H II regions. Evidence that the H II regions S254, S256, and S257 have had an important effect in shaping this cloud is apparent in Figures 1, 2, and 4 which show high-density gas outlining the southern boundaries of these H II regions, a configuration likely due to material swept up by these expanding H II regions.

A more predictable impact of high-mass star formation on the cloud is its effect on cloud disruption. Energetic stellar winds and expanding H II regions, both seen in the S254–S258 cloud, are likely to be the principle means by which molecular clouds are destroyed (Elmegreen and Lada 1977; Bally and Scoville 1980). The effect of the molecular outflow on the integrity of the cloud is expected to be minimal, since the gravitational energy of the cloud (7×10^{48} ergs) is much larger than the kinetic energy associated with the molecular outflow (2×10^{45} ergs). More significant to the cloud's evolution is the effect of the expanding H II regions. Currently, the spherical shape of the H II regions and the absence of molecular gas to the north of the cloud suggest that the H II regions have or will soon break through the northern surface of the cloud resulting in a rapid decompression of the gas within the H II region. The rocket phase that follows (Bally and Scoville 1980) may be one of the dominate forces which disrupt the cloud. Thus the ability of this cloud to continually form stars in the future is dependent upon the degree of disruption by events associated with past star-formation activity.

VI. CONCLUSION

The far-infrared and millimeter molecular line emission from the S254–S258 molecular cloud have been analyzed to investigate the coupling between the dust and gas components and the internal energetics associated with molecular clouds. The physical properties (temperature and column density) of the dust component have been estimated from fitting model intensities derived from a mass column density–temperature relationship to the observed far-infrared emission. A more complete accounting of the dust component, even at temperatures less than 20 K, is provided by modeling the far-infrared emission. A moderate correlation is found between the mass column density of the gas and the mass column density of the dust. This correlation suggests that the dust distribution is

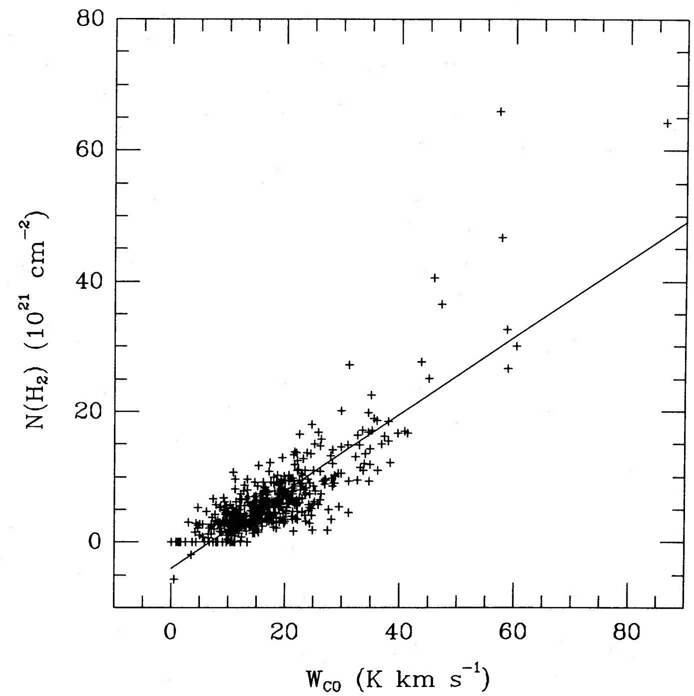

FIG. 14.—A point-to-point comparison between the molecular hydrogen gas column density inferred from ^{13}CO column densities and an abundance of ^{13}CO to H_2 of 1×10^{-6} and integrated ^{12}CO emission W_{CO}. The correlation suggests that W_{CO} can be used to trace gas column density. The conversion constant between $N(H_2)$ and W_{CO} is $(5.9 \pm 0.2) \times 10^{20}$ cm^{-2} (K km s^{-1})$^{-1}$.

an adequate tracer of cloud structure. The heating of the dust component is attributed to both the embedded newborn stars associated with embedded, compact H II regions and the stars responsible for three of the optical H II regions (S255, S257, and S258).

This work was supported in part by NSF grant AST 85-12903 to the Five College Radio Astronomy Observatory and the Astrophysics Data Program of the National Aeronautics and Space Administration.

APPENDIX

^{12}CO AS A TRACER OF MOLECULAR HYDROGEN MASS

The utility of integrated ^{12}CO $J = 1$–0 intensity as a tracer of molecular hydrogen has long been a subject of uncertainty since the opacity of this transition is very large. It is generally assumed that ^{13}CO emission is an adequate probe of cloud material based on the observed correlation between ^{13}CO intensity and visual extinction (Dickman 1978). Given the relative strengths between these two transitions and therefore the time required for observations especially in external galaxies, it is beneficial to establish the proper calibration between ^{12}CO emission and molecular hydrogen column density.

The observations presented in this study allow a detailed comparison of mass tracers derived from ^{12}CO and ^{13}CO emission respectively within an individual cloud. In addition, since extragalactic observations are possibly weighted toward warm regions similar to the S254–S258 cloud, such an analysis provides a useful check on the assumption often employed in using ^{12}CO emission. In Figure 14, a point to point comparison between the molecular hydrogen column density derived from equation (2) and the integrated ^{12}CO emission W_{CO} ($\int T(^{12}CO)dv$) is shown. A least-squares fit to the data provides the relationship

$$N(H_2) = (5.9 \pm 0.2) \times 10^{20} W_{CO} - (4.0 \pm 0.4) \times 10^{21} , \quad \text{(A1)}$$

with a correlation coefficient 0.84. The negative y intercept reflects the extended nature of ^{12}CO emission relative to ^{13}CO and that there are local regions within the cloud which are warm but are not enhanced in gas column density. However, in general, W_{CO} appears to be a good tracer of molecular gas column density over most of the projected surface of the molecular cloud. The conversion constant between $N(H_2)$ and W_{CO} is comparable to values derived by other independent methods within the range (1–6) $\times 10^{20}$ cm^{-2} (K km s^{-1})$^{-1}$ (Bloeman 1987).

REFERENCES

Bally, J., and Lada, C. 1983, *Ap. J.*, **265**, 824.
Bally, J., and Scoville, N. Z. 1980, *Ap. J.*, **239**, 121.
Beichman, C. A., Becklin, E. E., and Wynn-Williams, C. 1979, *Ap. J.* (*Letters*), **232**, L47.
Bloeman, H. 1987, in *Interstellar Processes*, ed. D. J. Hollenbach and H. A. Thronson (Dordrecht: Reidel), p. 143.
Bohlin, R. C., Savage, B. D., and Drake, J. F. 1978, *Ap. J.*, **224**, 132.
Boulanger, F., Beichman, C., Desert, F. X., Helou, G., Perault, M., and Ryter, C. 1988, *Ap. J.*, **332**, 328.
Boulanger, F., and Perault, M. 1988, *Ap. J.*, **330**, 964.
Dickman, R. L. 1978, *Ap. J. Suppl.*, **37**, 407.
Draine, B. T. 1985, *Ap. J. Suppl.*, **57**, 587.

Draine, B. T., and Anderson, N. 1985, *Ap. J.*, **292**, 494.
Elmegreen, B. G., and Lada, C. 1977, *Ap. J.*, **214**, 725.
Evans, N. J. II., Blair, G. N., and Beckwith, S. 1977, *Ap. J.*, **217**, 448.
Goldreich, P., and Kwan, J. 1974, *Ap. J.*, **189**, 441.
Heyer, M. H., Vrba, F. J., Snell, R. L., Schloerb, F. P., Strom, S. E., Goldsmith, P. F., and Strom, K. M. 1987, *Ap. J.*, **321**, 855.
Hildebrand, R. H. 1983, *Quart. J.R.A.S.*, **24**, 267.
Ho, P., Martin, R., and Barrett, A. 1981, *Ap. J.*, **246**, 761.
Huang, Y.-L., and Thaddeus, P. 1986, *Ap. J.*, **309**, 804.
IRAS Point Source Catalog 1985, Joint *IRAS* Science Working Group (Washington, DC: US Government Printing Office).
Israel, F. P. 1976, *Astr. Ap.*, **52**, 175.
Jaffe, D. T., Davidson, J. A., Dragovan, M., and Hildebrand, R. H. 1984, *Ap. J.*, **284**, 637.
Kutner, M. L., and Ulich, B. L. 1981, *Ap. J.*, **250**, 341.
Lada, C. J. 1985, *Ann. Rev. Astr. Ap.*, **23**, 267.
Lizano, S., and Shu, F. H. 1988, *Ap. J.*, preprint.
Lo, K. Y., and Burke, B. F. 1973, *Astr. Ap.*, **26**, 487.
Lonsdale, C. J., Helou, G., Good, J. C., and Rice, W. L. 1985, *Cataloged Galaxies and Quasars Observed in the IRAS Survey* (Washington: US Government Printing Office), p. B1.
Loren, R. B. 1976, *Ap. J.*, **209**, 466.
Mathis, J. S., Rumpl, W., and Nordsieck, K. H. 1977, *Ap. J.*, **217**, 425.
Mezger, P. G., Chini, R., Kreysa, E., Wink, J. E., and Salter, C. J. 1988, *Astr. Ap.*, **191**, 44.
Moneti, A., Pipher, J., Helfer, H. L., McMillan, R. S., and Perry, M. L. 1984, *Ap. J.*, **282**, 508.
Mooney, T. J., and Solomon, P. M. 1988, *Ap. J.* (*Letters*), **334**, L51.
Puget, J. L., Leger, A., and Boulanger, F. 1985, *Astr. Ap.*, **142**, L19.
Purcell, E. M. 1976, *Ap. J.*, **209**, 685.
Richardson, K. J., White, G. J., Gee, G., Griffin, M. J., Cunningham, C. T., Ade, P. A. R., and Avery, L. W. 1985, *M.N.R.A.S.*, **216**, 713.
Scoville, N. Z., and Good, J. C. 1987, *Star Formation in Galaxies*, ed. C. J. Lonsdale (Washington: US Government Printing Office), p. 3.
Scoville, N. Z., Sanders, D. B., and Clemens, D. P., 1986, *Ap. J.* (*Letters*), **310**, L77.
Scoville, N., and Kwan, J. 1976, *Ap. J.*, **206**, 718.
Sharpless, S. 1959, *Ap. J. Suppl.*, **4**, 257.
Snell, R. L., and Bally, J. 1986, *Ap. J.*, **303**, 683.
Snell, R. L., Heyer, M. H., and Schloerb, F. P. 1989, *Ap. J.*, **337**, 739.
Ungerechts, H., and Thaddeus, P. 1987, *Ap. J. Suppl.*, **63**, 645.

MARK H. HEYER: Department of Astronomy and Astrophysics, University of Pennsylvania, David Rittenhouse Laboratory, Philadelphia, PA 19104–6317

JAMES MORGAN, F. PETER SCHLOERB, and RONALD L. SNELL: Five College Radio Astronomy Observatory, Lederle Research Tower, University of Massachusetts, Amherst, MA 01003